Spatial Distribution of DNA Double-Strand Breaks from Ion Tracks

A. Hauptner[1], W. Friedland[2], S. Dietzel[3], G.A. Drexler[4], C. Greubel[5], V. Hable[5], H. Strickfaden[3], T. Cremer[3], A.A. Friedl[4], R. Krücken[1], H.G. Paretzke[2] and G. Dollinger[5,*]

[1]Physik Department E12, TU-München
D-85748 Garching, Germany
[2]Institut für Strahlenschutz, GSF
D-85764 Neuherberg, Germany
[3]Department Biologie II, LMU-München
D-82152 Martinsried, Germany
[4]Strahlenbiologisches Institut, LMU-München
D-80336 München, Germany
[5]Angewandte Physik und Messtechnik, LRT2, UniBw-München
D-85577 Neubiberg, Germany

Abstract

Theoretical and experimental approaches are developed to investigate the spatial distribution of DNA damage induced by energetic ions in cell nuclei, with a special emphasis on DNA double-strand breaks (DSB). Using a phenomenological description for the relationship between energy dose and DSB induction, the total number of DSBs and their average number per unit pathlength can be calculated analytically for single ion tracks in cell nuclei. A simple approach to microscopic DNA damage description is offered by analytical representations which give the average energy dose in dependence of the radial distance from the ion track. However, the extreme fluctuations in the DNA damage per volume, which is due to the inhomogeneous ionisation events of the individual secondary electron paths and the structure of chromatin in the nucleus, make a true follow-up of the ionisation and excitation events desirable, e.g. by using Monte Carlo methods. The visualisation of DSBs

* E-mail: guenther.dollinger@unibw.de

by staining proteins which accumulate in large amounts at DSB repair sites, thus forming so-called foci, allows to analyse the spatial distribution of DSB sites under the fluorescence microscope. With this method, generally a much lower number of DSB sites along an ion track is observed than expected on basis of calculations. This observation hints at insufficient consideration of gross structures in the organisation of nuclear DNA or at a fast clustering of DSBs, possibly to form repair factories.

Contents

1 Introduction **60**

2 Experimental Techniques **62**
2.1 Microirradiation of Cells by a High Energy Ion Microprobe 62
2.2 Optical Detection of DSB Sites in Cell Nuclei Using Immunofluorescence Technique 65

3 Microscopic DSB Distribution **65**
3.1 General Considerations 65
3.2 Radial Distributions of Energy Dose and DSBs 71
3.3 Influence of Chromatin Structure on DSB Distribution 74
3.4 Longitudinal DSB Distributions 77

4 Future Prospects **80**

Acknowledgements **83**

References **83**

1. Introduction

Double-strand breaks (DSBs) in the DNA are a major threat for each living cell since they affect the genome integrity. Ionising radiation is known to be one of the main elicitors of DSBs. Natural sources of ionising radiation are cosmic rays and radiation from radioactive isotopes in the environment (e.g. in minerals or in the atmosphere) or directly incorporated into living organisms, like ^{14}C or ^{40}K. Medical x-ray diagnostics, single photon emission computed tomography (SPECT) or positron emission tomography (PET), as well as tumour treatment by ionising radiation (x-rays, electrons, protons, heavy ions), are further sources of unintended or intended DSB induction. The number and the 3D arrangement of DSBs induced by a given dose are important quantities for the understanding of cellular reactions like DSB repair, programmed cell death (i.e. apoptosis) or

the induction of mutations. There are several models available which predict the spatial distribution of energy dose or of generated DSBs by analytical (Butz and Katz, 1967; Chatterjee and Schaeffer, 1976; Xapsos, 1992; Chen et al., 1994) or numerical (i.e. Monte Carlo calculation) (Krämer and Kraft, 1994; Nikjoo et al., 1999; Friedland et al., 2005) approaches. The latter models are mainly based on the simulation of primary ionisation and excitation processes, as well as the follow-up reactions from the interaction cascades of the secondary electrons. All relevant differential cross sections for ionisation and excitation as well as the angular and energy spectra of secondary electrons from the various interactions have to be known accurately for the detailed Monte Carlo studies. There has been substantial progress in the last years to include relevant cross section data (Dingfelder et al., 1998; Dingfelder, 2002) into Monte Carlo codes to calculate local dose and especially DSB distributions. However, there is still a lack of accuracy in the cross section data for heavy ion primary particles at energies where the stopping force (LET, linear energy transfer) is close to its maximum, and at lower energies. On the other hand, the most severe problem remains to model the chemical effects on DSB induction which result from radicals produced by the ionising radiation not directly on DNA sites. Since the DNA content in a cell nucleus is only a very small fraction of the total mass, molecules other than DNA, mainly water molecules, are much more likely to be hit by the radiation. In addition, a realistic model for the organisation and structure of the DNA within the cell nucleus is needed in order to calculate accurate DSB distributions from such a bottom-up approach.

From the experimental side, the recently developed high energy ion microprobes offer new possibilities to investigate ion track structures in cell nuclei with respect to DSB production, the ensuing dynamics of DSB sites, and the complex spatio-temporal behaviour of proteins and chromatin modifications involved in DSB repair.

In this work we want to present some theoretical aspects and experimental findings on how DSBs are distributed around and along an ion track. We will first present how individual cells can be targeted by focussed ions at a high energy ion microprobe and how double-strand breaks can be visualised in cells. In a second part, we will describe the analytical and numerical approaches to calculate local dose and DSB distributions. The aim is a comparison of the measured spatial distributions of DSB sites with the calculated distributions, in order to further understand the processes of DNA damage induction in biological systems after ion irradiation.

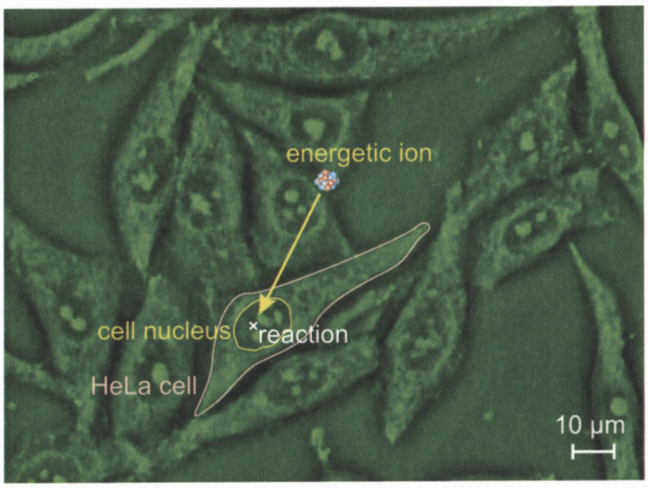

Figure 1. Micrograph of living HeLa cells in optical phase contrast. The nucleus of one cell is schematically subjected to a single ion hit.

2. Experimental Techniques

2.1. Microirradiation of Cells by a High Energy Ion Microprobe

The purpose of a microirradiation experiment on living cells is to target a certain position within a cell by a definable amount of ionising radiation damage. Especially the cell nucleus, which contains the genetic material DNA, represents the object of radiobiological interest (Figure 1). Ion microprobes allow to target sub-cellular structures by a single or a counted number of ions. To do so, high energy ions are focussed to beam spots well below 1 μm in diameter, for example by a set of magnetic quadrupole lenses (Fischer, 1985; Datzmann et al., 2001; Greif et al., 2004). A less expensive arrangement with a resolution of only about 2 μm employs microcollimators (Folkard et al., 1997a; Randers-Pehrson et al., 2001). As an example for a focussing ion microprobe the Munich microprobe setup SNAKE (Superconducting Nanoprobe for Applied nuclear (Kern-) physics Experiments) and the corresponding cell irradiation technique are described here. The schematic ion beam transport system of SNAKE (and in principle of comparable microprobes) is shown in Figure 2. An ion beam well-defined with respect to beam energy, charge state and mass is prepared using a 90° magnet located behind a high energy ion accelerator. With a system of precision slits the ion beam is trimmed, thus forming the object for an ion optical transformation and defining the aperture of the beam. The result of this beam trimming is a flow of

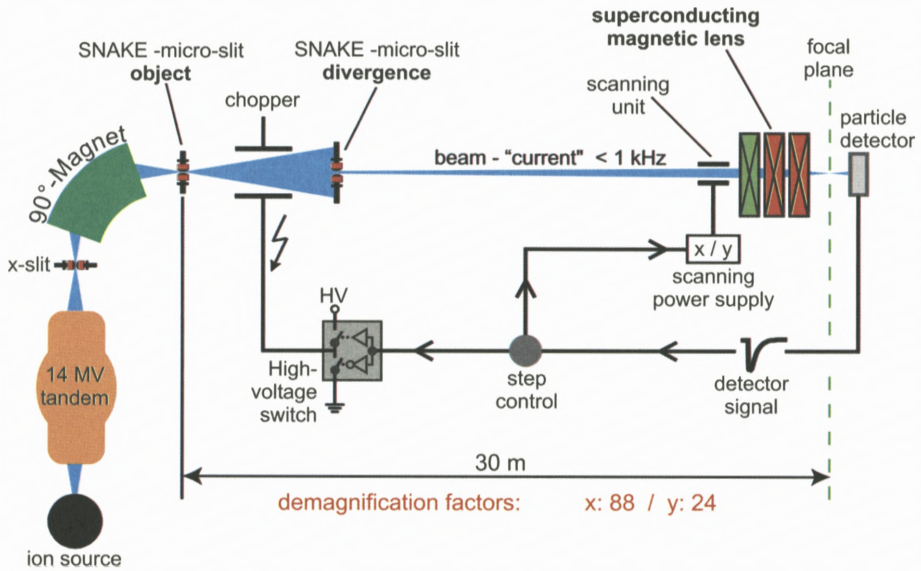

Figure 2. Beamline system of the ion microprobe SNAKE at the Munich tandem accelerator.

ions with a particle rate of not more than 10^3 per second, which then is focussed by a superconducting magnetic lens into the focal plane of the microprobe. An electrostatic scanning unit in front of the magnetic lens allows to scan the beam focus over the target without moving the sample mechanically. In order to irradiate samples with defined numbers of ions the described beam transport system is completed with an electrostatic beam shutter (chopper) enabling on-off-switching times in the order of 1 μs.

As living cell samples can only be handled under normal atmospheric pressure, the ion beam has to leave the vacuum of the beam transport line for cell irradiation. To separate vacuum from atmosphere, thin foils (e.g. made of Kapton or silicon nitride) are used which are traversed by the ion beam. The ion energy has to be sufficiently high to limit the lateral straggling caused by small angle scattering and to ensure a sufficient penetration depth in matter.

Suitable cell chambers have to be designed to make the cells accessible for the ion beam while ensuring favourable culture conditions (see an example in Figure 3). In general, these chambers contain a thin polymeric foil (e.g. Mylar foil) on which the cells are grown. For the detection of energetic ions during irradiation of cells different concepts exist. The three most common concepts base upon the detection of secondary electrons from the inner wall of vacuum windows (Fischer et al., 2003), the scintillation light of thin plastic foils placed in front of the cell

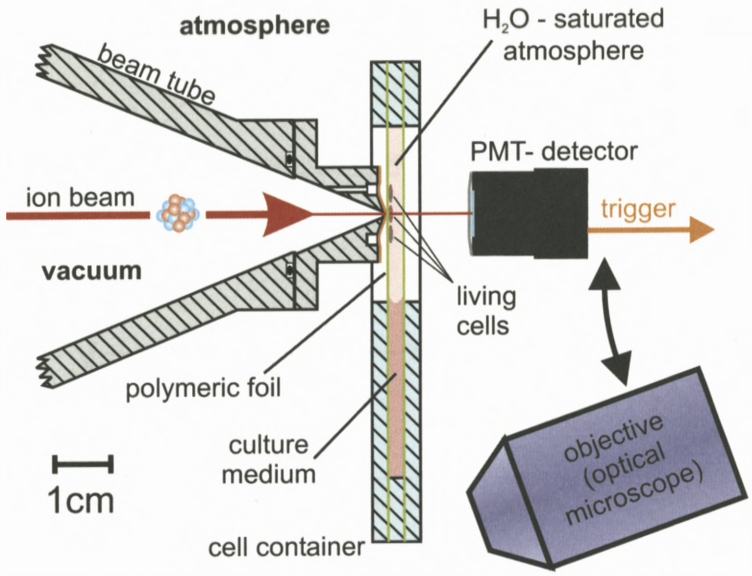

Figure 3. Arrangement for microirradiation of living cells with energetic ions. The ion beam exits the vacuum system through a bore in the beam tube covered by a thin foil. This vacuum window touches the back side of the cell carrier, polymeric foil to reduce beam spot broadening caused by angular scattering of the beam.

sample (Folkard et al., 1997b), or the ion-stop detection in a silicon or scintillation detector behind the sample (Hauptner et al., 2004). In the SNAKE setup the latter concept is realised. Detecting each ion on its arrival, the beam to the target can be switched off after a certain number of counted ions, e.g. after the first ion, and using the beam scanning unit (Figure 2) the ion beam can be directed to a new position, to which the next ion will be delivered. To perform targeted irradiations of cellular structures, an optical microscope has to be integrated into the irradiation setup. At present, the Munich irradiation configuration uses a standard inverted optical microscope devised for cell biology applications. With the help of this instrument the optical focussing of the ion beam on a fluorescent screen is performed, as well as the positioning of target locations relative to the beam position.

In order to study the DNA damage structure along the ion tracks (see Section 3.4), it is advantageous to perform irradiation experiments with a small angle between ion beam direction and the carrier foil of the cells (Jakob et al., 2003; Aten et al., 2004). Due to the optical properties of the analysing fluorescence microscope with the optical axis perpendicular to the cell substrate, a much better resolution along the track direction is obtained with this kind of irradiation

geometry than with the placement of the specimen perpendicular to the ion beam described above. At the Munich setup cells can be irradiated with an angle of 10° between beam direction and carrier foil. However, with this setup the ability to perform targeted irradiation is lost due to angular scattering and the large distance between vacuum exit window and target.

2.2. Optical Detection of DSB Sites in Cell Nuclei Using Immunofluorescence Technique

The induction of a DSB in the DNA of a living cell is a process taking place on the molecular level. A direct observation of a DSB using optical microscopy or electron microscopy is not possible due to lack of resolution and unsuitable sample structure. Visualisation of regions containing DSBs has, however, recently become possible with the help of cell biology and fluorescence microscopy methods. The first step in this procedure is done by the living cells themselves, which accumulate repair factors (proteins) at the sites of DSBs in order to initiate and execute repair of damaged DNA molecules. The experimenter can then fix the cells, i.e. kill them while preserving the biological structure, and treat them with antibodies which enter the cell nucleus. These primary antibodies are chosen to specifically recognize and bind to selected repair factors. Then secondary antibodies carrying a fluorescent dye molecule are added which bind to the primary antibodies (see schematic sketch in Figure 4a). Using an optical fluorescence microscope the distribution of the secondary antibodies and therefore of DSB sites in the form of so-called fluorescence foci can be observed with a resolution of about 200 nm (see Figure 4b).

In the near future, repair factors stained by green fluorescent proteins (GFP) will be used to follow DNA repair dynamics also in living cells on site at the ion microirradiation setup of SNAKE.

3. Microscopic DSB Distribution

3.1. General Considerations

It has been known for several decades that the biological effects of ionising radiation, such as cell killing or mutation, depend mainly on the energy dose $D = E/m$ (measured in Gy = J/kg), that is the ratio of the energy E deposited into a certain volume to its mass m. Scaling this quantity down to the cellular or subcellular level leads to so-called microdosimetry (Figure 5). As an extrapolation of the macroscopic dose, a local dose D_{loc} is defined as $D_{\mathrm{loc}} = \mathrm{d}E/\mathrm{d}m$ when the amount of energy $\mathrm{d}E$ is delivered into an infinitesimal small volume of mass $\mathrm{d}m$.

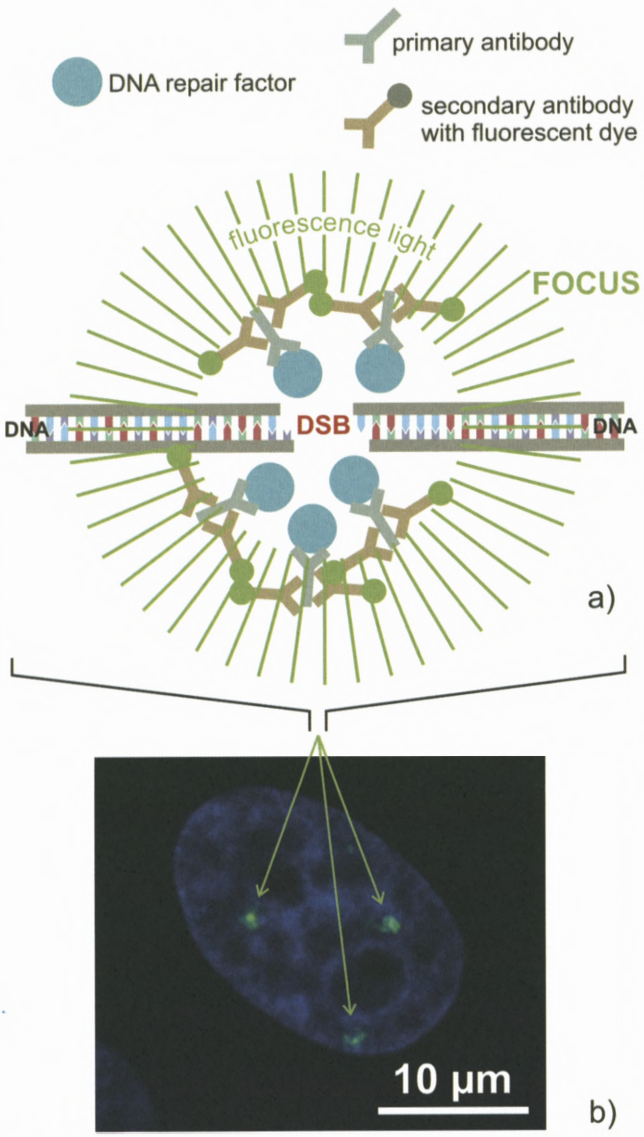

Figure 4. (a) DNA repair factors accumulating at DSB sites are marked with fluorescent antibodies (schematic drawing, not to scale). (b) Optical micrograph of a HeLa cell nucleus irradiated by single 55 MeV ^{12}C ions. The direction of the ion tracks is perpendicular to the image plane shown. Accumulated 53BP1 repair proteins are made visible as bright foci (green colour, see arrows) using immunofluorescence technique. The chromatin in the cell nucleus is marked by DAPI-counterstaining (blue colour) of DNA. The image is taken from an image stack (i.e. several optical slices perpendicular to the line of sight). Deconvolution software was used to reconstruct unmixed image information of single optical slices.

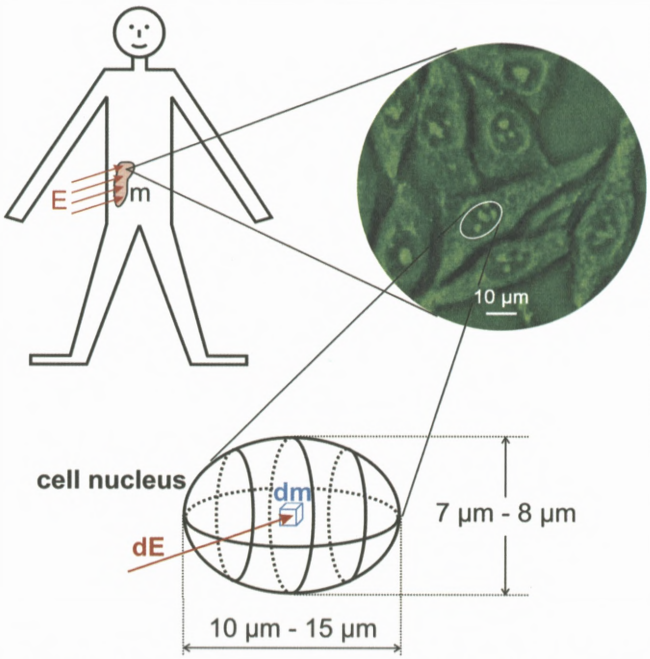

Figure 5. From macro- to micro-dosimetry: The mass element, in which one regards the deposition of radiation energy is scaled to a subcellular size.

X-ray and γ-ray irradiation damages living cells through the tracks of energetic electrons released mainly due to Compton scattering and photo effect. This so-called sparsely ionising radiation yields about $Y_{\mathrm{SSB}} = 1000$ single-strand breaks (SSBs) per Gy and about $Y_{\mathrm{DSB}} = 35$ DSBs per Gy within a diploid mammalian cell nucleus (Hall, 2000), over a wide range of absorbed doses. Using this linear relationship between energy dose and DSBs, a given local dose distribution $D_{\mathrm{loc}}(\mathbf{r})$ would result in a number $N_{\mathrm{DSB},\gamma}$ of induced DSBs within a certain voxel volume V_{Vox}:

$$N_{\mathrm{DSB},\gamma} = \frac{Y_{\mathrm{DSB}}}{V_{\mathrm{nucl}}} \int_{V_{\mathrm{Vox}}} D_{\mathrm{loc}}(\mathbf{r})\,\mathrm{d}V. \tag{1}$$

Using this equation one should obtain reasonable results as long as V_{vox} is sufficiently large so that it contains the average DNA concentration as found in the whole cell nucleus. V_{nucl} is the volume of the cell nucleus. For HeLa cells,[1] we have determined $V_{\mathrm{nucl}} = 710\ \mu\mathrm{m}^3$ (i.e. 0.71 ng of mass) on average, by measuring

[1] HeLa cells are immortalised human cells often used for biological experiments.

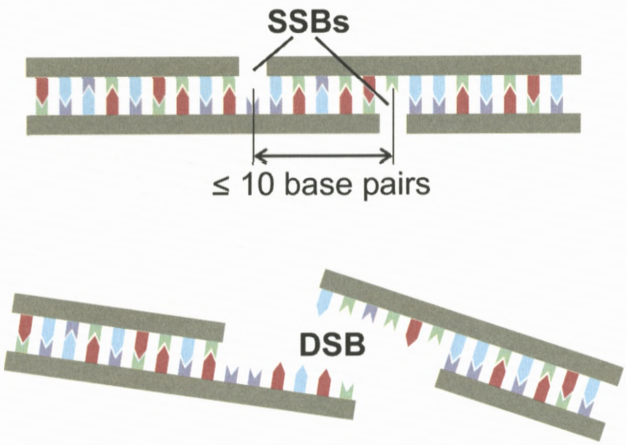

Figure 6. Generation of a double-strand break (DSB) from adjacent single-strand breaks (SSBs) on opposite strands of the DNA molecule.

a set of hundred HeLa cell nuclei using optical microscopy. Thus, an average dose of 1 Gy deposits an energy of 0.71 pJ into a HeLa cell nucleus. After irradiation with ions, the number of DSBs induced per unit dose may differ from that observed after X- or γ-irradiation. Thus, the ions' relative biological effectiveness for DSB induction, $\mathrm{RBE}_{\mathrm{DSB}}$, has to be considered in the determination of $N_{\mathrm{DSB,ion}}$, yielding

$$N_{\mathrm{DSB,ion}} = \frac{Y_{\mathrm{DSB}}\mathrm{RBE}_{\mathrm{DSB}}}{V_{\mathrm{nucl}}} \int_{V_{\mathrm{Vox}}} D_{\mathrm{loc}}(\mathbf{r})\,\mathrm{d}V = \mathrm{RBE}_{\mathrm{DSB}} N_{\mathrm{DSB},\gamma}. \tag{2}$$

DSBs occur if there are two SSBs on opposite strands on a DNA molecule within a distance smaller than 10 base pairs (i.e. 3 nm distance, see Figure 6). The probability for generation of two SSBs in close vicinity will be increased at sites of high local dose. Therefore, $\mathrm{RBE}_{\mathrm{DSB}}$ values are expected to exceed unity when the stopping force of the ions is close to or larger than the stopping force of electrons at their stopping force maximum (26 keV/μm). The effects from nuclear energy transfers, which are important for fast neutrons or slow ions, have to be treated differently, but little is known about dose-DSB relationships from atomic knock-on collisions.

A swift ion loses the energy $\Delta E = \int_{\ell}(\mathrm{d}E/\mathrm{d}x)\,\mathrm{d}x$ when it passes through a cell nucleus along a path of length ℓ. If the ion is fast enough (specific energies larger than 1 MeV/nucleon), the stopping force $\mathrm{d}E/\mathrm{d}x$ within one cell is nearly

constant and is dominated by electronic interaction. Thus, the energy deposited in the nucleus can be approximated by

$$\Delta E = \frac{\mathrm{d}E}{\mathrm{d}x}\,\ell, \tag{3}$$

where ℓ is the length of the track in the cell nucleus. On the other hand, if ion velocities are not too high (i.e. less than 20 MeV/nucleon), the secondary electrons ejected along the ion track in a cell nucleus are mostly stopped within that cell nucleus, and the energy ΔE is fully deposited there. Although the ions' nuclear energy loss may show enhanced biological effectiveness compared to electronic energy loss, these effects should be negligible at high ion energies since only about 0.1% of the energy loss is of nuclear origin.

The average height of a HeLa cell nucleus grown on foil was determined as 7.6 μm. If this nucleus is traversed perpendicularly to the substrate by a swift ion, an average dose D_{av} is deposited in the cell nucleus (mass density approximated by $\rho_{\mathrm{H_2O}}$) of mass m_{nucl}:

$$D_{\mathrm{av}} = \frac{\Delta E}{\rho_{\mathrm{H_2O}} V_{\mathrm{nucl}}} = \frac{\Delta E}{m_{\mathrm{nucl}}}\,. \tag{4}$$

Thus, the number $N_{\mathrm{DSB,ion}}$ of DSBs obtained from a single ion passage through a cell nucleus is given by:

$$N_{\mathrm{DSB,ion}} = D_{\mathrm{av}} Y_{\mathrm{DSB}} \mathrm{RBE}_{\mathrm{DSB}}. \tag{5}$$

The energy deposition in a HeLa cell nucleus, the average energy dose D_{av} and the numbers of DNA strand breaks when applying uniformly the dose effect relationship for sparsely ionising radiation created by the passage of a single particle through a cell nucleus are plotted in Figure 7 for various kinds of ions and in addition for electrons in dependence of their velocity. Dividing N_{DSB} by the average height of the nucleus, one obtains the number of DSBs per unit path length of the particle (see rightmost scale in Figure 7). This number varies over orders of magnitude from less than 0.01 DSBs averaged per micrometer for protons with more than 100 MeV energy to about 100 DSBs per micrometer (and even more considering $\mathrm{RBE}_{\mathrm{DSB}}$ values) for the heaviest ions around their stopping force maximum.

Fast protons have stopping forces close to those of energetic electrons at the same speed, while the stopping forces of heavier ions exceed it by several orders of magnitude. The most severe difference between sparsely ionising radiation and heavy projectiles penetrating tissue lies in the local energy deposition around the ion track. This results in high local doses in the vicinity of the ion track in the

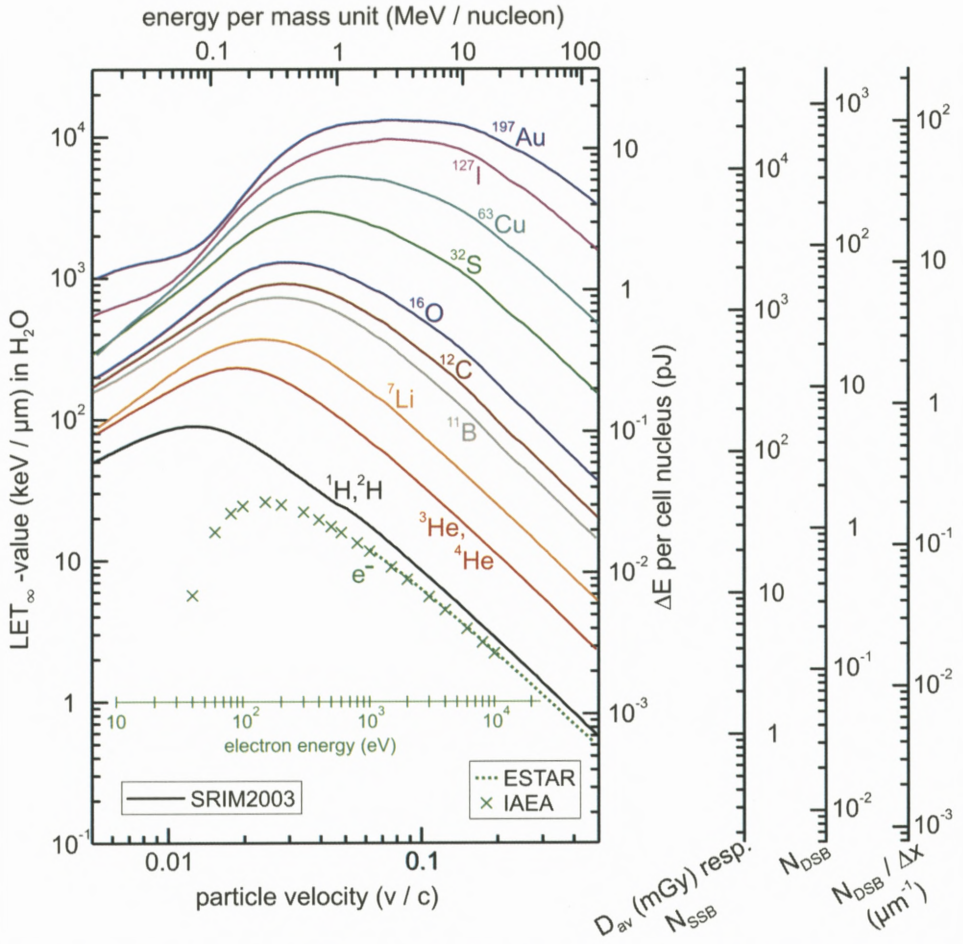

Figure 7. Damage induction in cell nuclei for single hits of different ions and electrons: The amount of energy ΔE deposited in the nucleus assumes a particle track length of 7.6 μm within the nucleus. The additional precondition for the average energy dose D_{av} is a cell nucleus mass of 0.71 ng. The numbers of SSBs N_{SSB} and DSBs N_{DSB} are obtained by a strict scaling as known from sparsely ionising radiation. Especially for DSB induction at heavy ion tracks the values shown do not consider enhanced effectiveness (i.e. $RBE_{DSB} = 1$ for all values shown). Note also that for the lower particle energies shown the stopping force value (LET_∞) cannot be assumed to be constant along the track through the whole cell nucleus. In that case, the absolute values shown for energy deposition, average dose and numbers of strand breaks are not applicable. Stopping force data were taken from SRIM (Ziegler and Biersack, 2003) for ions and from IAEA (1995) as well as from ESTAR (Berger et al., 2005) for electrons.

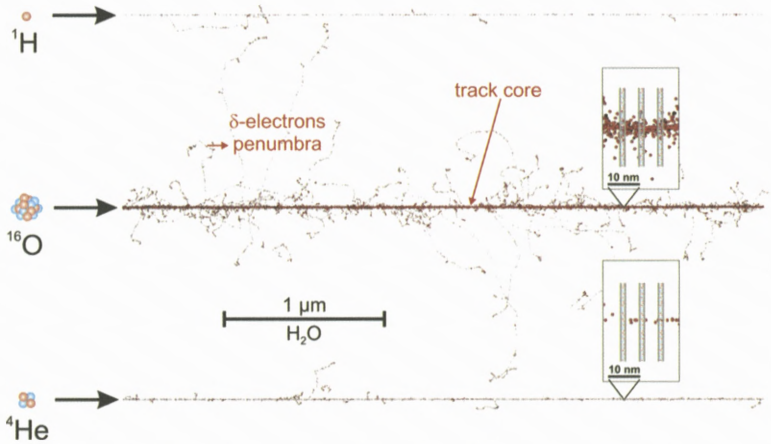

Figure 8. Projections of PARTRAC calculations (ionisation and excitation events in water) for three different ion tracks with the same specific energy 6.25 MeV/nucleon. The magnified cut-outs with overlaid DNA (schematic) demonstrate the difference between densely and sparsely ionising radiation.

case of heavy ions, while sparsely ionising radiation creates fluctuations of dose only through the statistical nature of electron trajectories and their ionisation and excitation processes.

3.2. Radial Distributions of Energy Dose and DSBs

The local dose distribution has been subject to various theoretical approaches. The most detailed calculations stem from Monte Carlo simulations where the primary reactions of the ion along its trajectory are calculated in a statistical way and the probability for a reaction to happen is calculated from the relevant differential cross sections (Dingfelder et al., 1998; Dingfelder, 2002). A snap shot of the ionisation and excitation events along charged particle tracks in water as target material is plotted in Figure 8. It has been projected from a 3D Monte Carlo calculation with the code PARTRAC (Friedland et al., 1998, 1999, 2003), applied to a proton, an oxygen and a helium ion, respectively, at a specific energy of 6.25 MeV/nucleon, corresponding to a velocity of $0.115c$, where c is the speed of light. While especially for the proton track the single events along the center of the track (= core) can be resolved on the given scale, a continuous ionisation path is generated by the oxygen track where an ionisation is created within every atomic distance. Ionisation paths are also visible where secondary electrons carry some energy leading to ionisations at larger distances from the core. This more sparsely ionised region around the track core is sometimes called "penumbra".

Although the average dose is smaller by orders of magnitudes in the penumbra than in the core, there are areas of relatively high dose close to the ends of the secondary electrons paths, where the highest stopping force of electrons occurs (see Figure 7). At these end points the ionisation density is high enough that there also exists a significant probability for DSB induction. A number of radicals is also formed from various molecules besides the DNA molecules, which can potentially create additional DSBs.

Monte Carlo simulations are laborious, and for certain applications it may be helpful to estimate the average energy dose at a given radial distance to the ion track center using an analytical expression. Analytical models have already been used for longer times for the calculation of microscopic dose distributions. Microdosimetry experiments were performed, where ionisation doses were measured in diluted gases and scaled to fluid water densities. Therewith dose distributions have been seen to scale with $1/r^2$ with r being the radial distance from the ion track core. Several analytical representations of such dose distributions were given by Butz and Katz (1967), Chatterjee and Schaeffer (1976), Xapsos (1992) and Chen et al. (1994). For some of them it is argued, that the energy deposited should be divided equally between core and penumbra region, which leads to some incongruities in the radial dose distribution at the core/penumbra interface (Chatterjee and Schaeffer, 1976). For other representations less crude assumptions on the track core are made (Butz and Katz, 1967). In general, comparisons of the analytical representations with the Monte Carlo calculations show quite good agreement in the penumbra region, where all calculations are also in good agreement with measured data. The agreement is, however, less favourable in the core region and also at the very far distances, where the $1/r^2$ scaling ends. There, the analytical representations assume a sharp drop while the Monte Carlo calculations show only a faster decrease in dose. This decrease may be approximated by a $1/r^4$ scaling.

Using this approximation, an improved analytical representation was fitted to Monte Carlo simulation data of average radial dose distributions in water (Krämer and Kraft, 1994) for high ion energies ($E/A > 1$ MeV/nucleon):

$$D = \begin{cases} \frac{B}{r} & r \le r_i \\ \frac{Br_i}{r^2} & r_i < r \le r_k \\ \frac{Br_i r_k^2}{r^4} & r_k < r \le r_{\max} \\ 0 & r > r_{\max} \end{cases} \quad \text{with the radii} \quad \begin{aligned} r_i &= 1 \text{ nm} \\ r_k &= 45 \text{ nm}(E/A)^{1.75} \\ r_{\max} &= 5r_k \end{aligned} \tag{6}$$

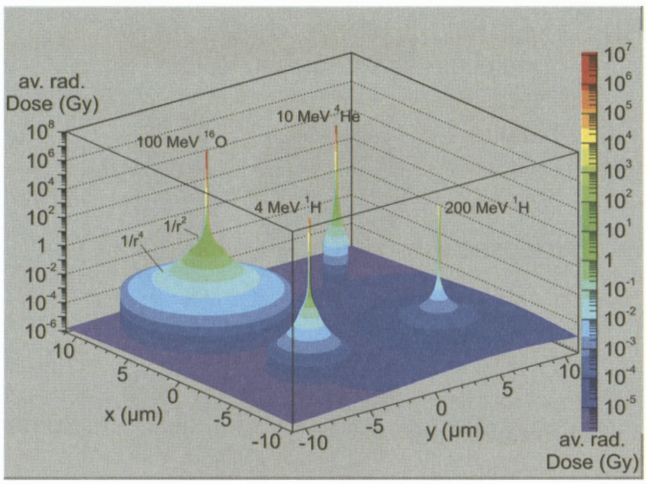

Figure 9. Average radial dose distributions given by Equation (6) for four different ions with track directions perpendicular to the x–y plane. Looking at the dose distribution of 100 MeV ^{16}O one can distinguish between the two different radial dependences ($1/r^2$ and $1/r^4$, respectively) used in the analytical expression. The dose background over the whole area shown originates from the track of the fast 200 MeV proton. To avoid an infinite high dose in the center of the tracks the dose has been restricted to B/(0.1 nm) in the track centers. Because of graphical reasons the drawn surfaces near the track centers were radially expanded and are not to scale. Moreover, one should always keep in mind that the average radial dose distributions shown in this figure veil the stochastic nature of energy deposition due to the tracks of secondary electrons (compare Figure 8).

with

$$B = \frac{1}{\rho_{H_2O}} \frac{dE}{dx} \frac{1}{2\pi r_i (5.28 + 1.75 \ln(E/A))} ,$$

$\rho_{H_2O} = 1.0$ g/cm^3 and $E/A =$ kinetic energy divided by the mass of the particle measured in MeV/nucleon.

One has to be aware that, outside the core and up to r_k, the integrated radial dose scales with $\ln(r)$ due to the $1/r^2$ dependence of the radial dose distribution. Thus a significant fraction of the energy is deposited in that region. Since the end point r_k of the $1/r^2$ scaling increases disproportionate to the ion velocity ($r_k \sim (E/A)^{1.75} \sim v^{3.5}$), the interaction volume, where DSBs are most likely generated, depends heavily on the ion velocity. The absolute dose values depend on the stopping force dE/dx of the ion which again is a function of ion velocity and scales close to Z^2 at high ion velocities (with $Z =$ atomic number). The unreal infinity of the given dose distribution at $r = 0$ is meaningless if doses in real voxel volumina are determined.

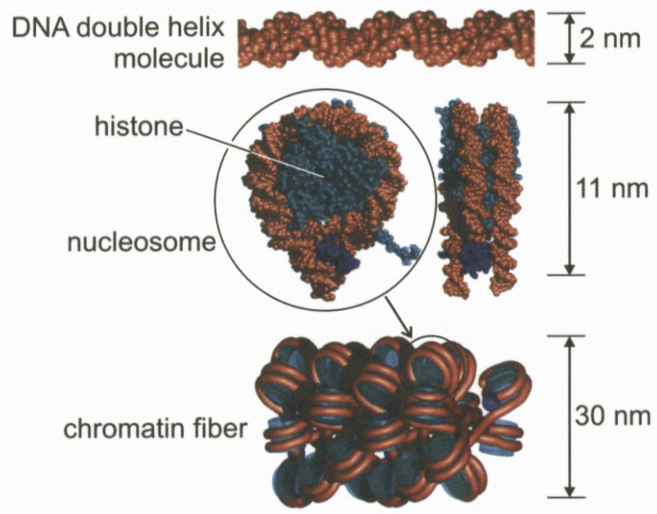

Figure 10. Organisation of the DNA molecule in nucleosomes where DNA is wrapped around histone proteins (side and front view, atomic resolution), and condensation of nucleosomes into the 30 nm chromatin fiber. This photorealistic visualisation was copied from the work of Bernhardt (2002).

In order to illustrate the situation for different ions, the average radial dose distributions according to Equation (6) are plotted in Figure 9. Assuming a strict linear dose – DSB relationship and knowing the corresponding RBE_{DSB} values (e.g. from experiments) one could scale these distributions also to average radial DSB distributions. Note that the diameter $2r_k$ exceeds the diameter of a normal cell nucleus of about 10 μm at energies exceeding 20 MeV/nucleon. At those high energies the total number N_{DSB} of DSBs created in a cell nucleus traversed by a single ion is lower than calculated based on Equations (3–5) since a fraction of the energy is deposited outside the cell nucleus.

3.3. Influence of Chromatin Structure on DSB Distribution

Since the damaging events are inhomogeneously distributed on a microscopic scale, Monte Carlo calculations offer the possibility for a detailed modelling of DSB distributions along the ion track and also of their radial distributions. To do so, a detailed model of the DNA and chromatin structure and its organisation within a cell nucleus is needed. In addition, all mechanisms, direct ionisation and excitation processes on DNA as well as the effects of radicals created by the radiation in the vicinity to a DNA molecule have to be taken into account. The

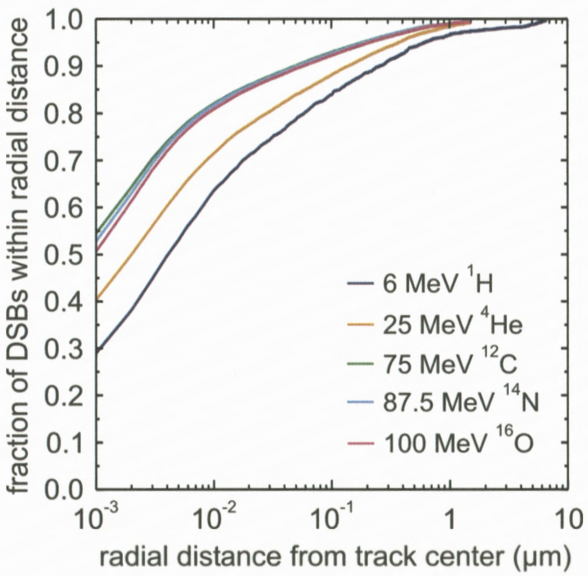

Figure 11. Average fraction of DSBs found within a given radial distance from the ion track center as calculated by the PARTRAC code for different ions with the same velocity.

microscopic double-helical structure of the DNA, its organisation around nucleosomes and its compaction into the 30 nm chromatin fibers are well investigated (Figure 10). To what degree higher order chromatin organisations are present in the cell nucleus, and how these structures look like, is still under discussion. From the total length of 30 nm chromatin fibers (5.5 cm) in a human cell (corresponding to 6×10^9 base pairs of DNA) the volume occupied by chromatin within one cell nucleus can be calculated to 39 μm^3. Regarding the average volume of the nucleus (710 μm^3) one can estimate that only about 5% of the cell nucleus is made of chromatin. The remaining space is filled mainly by water and an additional fraction of other organic molecules.

The current PARTRAC code assumes a homogeneous distribution of chromatin fibers in the cell nucleus. Basic elements are 150 nm long chromatin fiber rods arranged in rosette-like structures with stochastic variations (Friedland et al., 2003). Based on this model for a cell nucleus the PARTRAC code is able to calculate the spatial distribution of radiation induced DSBs. The average fraction of DSBs found within a given radial distance from the ion track center is plotted in Figure 11 for various ions which all have the same specific energy ($E/A = 6.25$ MeV/nucleon). Each curve is the average of 10000 individual ion trajectories for protons and alpha particles and 5000 trajectories for the heavier

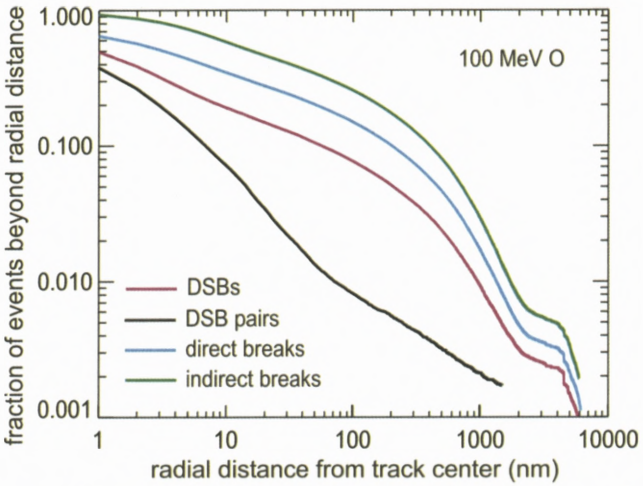

Figure 12. Average fraction of different DNA damage events generated beyond a given radial distance from a 100 MeV ^{16}O ion track center as calculated by the PARTRAC code. Each curve is normalised to a value of 1 for the track center (i.e. $r = 0$).

ions. The plots were normalised to an integrated value of 1 and have to be multiplied with the total number of DSBs created along a given ion track segment in order to obtain the average number of DSBs generated within the radius r. The calculations show that a significant proportion of the DSBs are found in the core region (i.e. 1 nm) but that there is still a considerable fraction of DSBs which is created at a distance from the core exceeding 100 nm. It is also remarkable that there is a difference in the DSB distribution for the heavier ions as compared to protons. The heavier ions have a higher relative yield for DSBs in or close to the core. This effect may be explained by the high density of damaging events induced by different primary or secondary reactions and which interact to enhance DSB induction in the core region. Speaking strictly in terms of RBE_{DSB} values a definition of radial dependent values $RBE_{DSB}(r)$ would be necessary with higher values for small radial distances. This means that a global scaling of radial dose distributions using an uniform RBE_{DSB} value as mentioned at the end of Section 3.2 is not expected to give accurate radial DSB distributions, especially not for heavy ion tracks. Besides radial distributions the PARTRAC calculation can also give an overview in which way DNA strand breaks are created (see an example for 100 MeV ^{16}O ions in Figure 12), whether by direct breaks from ionisation and excitation of the DNA molecules themselves or by indirect interaction from radicals produced mainly in water surrounding the DNA. The latter is about two times more efficient in damage creation than the direct processes (Michael and

O'Neill, 2000). Figure 12 shows in addition the fraction of DSBs and of DSB pairs generated beyond a given radial distance from the ion track center. A DSB pair consists of two lesions on the same modeled DNA fiber rod and constitutes an even more serious damage to the DNA than an isolated DSB. Since the DNA is organised in higher order structures the probability of creating a second lesion on the DNA molecule in close vicinity to another lesion is enhanced. This enhancement is especially prominent in the core of the ion track where the ionisation density is the highest. Thus, the radial distribution of DSB pairs decreases faster with increasing distance from the ion track center than the DSB distribution. Up to now, there is no experimental information available to prove and maybe to refine the predicted radial DSB and DSB pair distributions.

3.4. Longitudinal DSB Distributions

There would be a random distribution of DSBs in longitudinal direction along the ion track if the DNA molecules were distributed homogeneously inside the cell nucleus. However, the fiber structure of the chromatin exerts a strong influence on the longitudinal distribution of DSBs. In a first approximation the situation is illustrated in Figure 13. Here schematic chromatin fibers without internal structure are projected from a cuboid (1 μm $\times$ 1 μm lateral, 300 nm projected onto image plane) assuming a statistical distribution of the fibers within the volume. The ionisation track structure of a 100 MeV oxygen ion is overlaid onto this chromatin distribution. The probability that the ion passes directly through a chromatin fiber is low, but if it hits a fiber it produces a DSB cluster, which means several DSBs in close vicinity which are separated by a larger distance from the next DSB cluster. Some additional DSBs are created at larger radial distances from the ion path when secondary electron cascades end in or close to a DNA fiber. It is important to note that in reality the 30 nm fiber is arranged in a higher-order conformation, which as yet is not characterised. Already in Figure 4b it is evident that the chromatin is not distributed homogeneously inside the cell nucleus.

Experimental analysis of repair factor foci by conventional optical microscopy cannot resolve reliably the individual DSBs within one DSB cluster, due to the ultimate resolution of optical microscopy (200 nm) and the repair factor dependent extension of the fluorescent foci ($\approx$1 μm). Thus, the number of visible foci corresponding to DSB clusters or sufficiently separated DSB sites (i.e. $\approx$1 DSB), respectively, is expected to be lower than the calculated number of DSBs. The number of DSB clusters can also be estimated from the PARTRAC code. In our analysis we put all DSBs into one cluster which are generated on one 150 nm long fiber section (corresponding to 1.8×10^4 base pairs). Figure 14 shows, for a variety of ions and ion energies, the numbers of DSBs per path length expected when

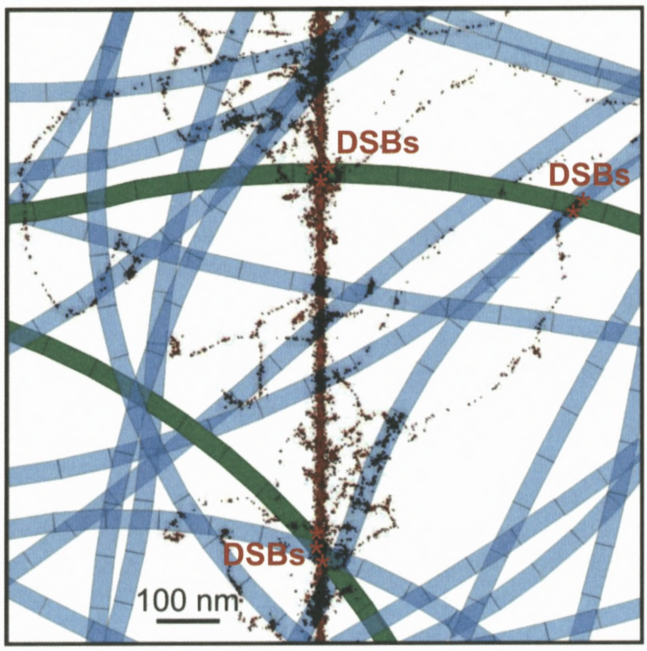

Figure 13. Illustrative visualisation of DSB and DSB-cluster induction along the track of an energetic ion. The projection of a 100 MeV ^{16}O ion track structure (PARTRAC) is overlaid on a simple model for a cell nucleus containing homogeneously distributed chromatin fibers. The fibers occupy a volume fraction of about 5%. A 300 nm thick layer of this model is projected perpendicularly to the image plane. Green marked fiber sections are thought to be directly hit by the ion track center.

assuming the linear extrapolation from sparsely ionising radiation (left column). The middle column shows the numbers of DSBs per path length as calculated from the PARTRAC code, which demonstrates an increased formation of DSBs due to the high ionisation density in the core region of the heavier ions. The relative biological effectiveness for DSB induction, RBE_{DSB}, was found to lie between $RBE_{DSB} = 1.3$ for 6.25 MeV protons and $RBE_{DSB} = 2.6$ for 75 MeV carbon and comparable ions. For comparison, experimentally determined RBE_{DSB} data ranging from 1.2 (for 21 MeV protons) to 2.8 (for 65.6 MeV oxygen ions) are also shown. These data were deduced from a comparison of experimentally obtained DNA fragment-size distributions with the outcome of simulations based on an analytical model for the radial dose distribution and Monte Carlo models for the distribution of chromatin in the nucleus (Friedl et al., 2003). The numbers of DSB clusters per path length, as determined by the PARTRAC code, are shown in the right column in Figure 14. For the densely ionising tracks of heavy ions where a strong clustering of DSBs can be expected these numbers are even lower than the

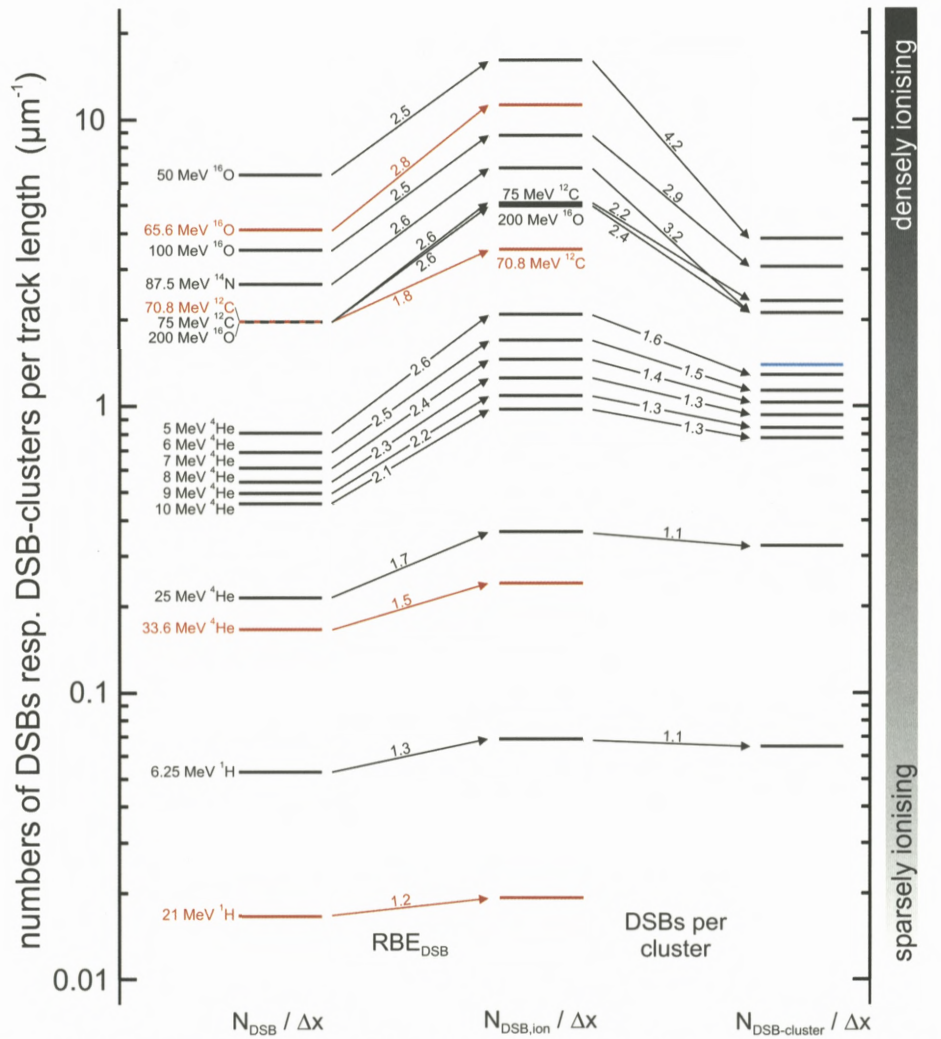

Figure 14. Left column: numbers of DSBs per ion track length ($N_{\mathrm{DSB}}/\Delta x$) for different ions obtained by extrapolating from sparsely ionising radiation (i.e. $\mathrm{RBE}_{\mathrm{DSB}} = 1$). Middle column: numbers of DSBs per ion track length ($N_{\mathrm{DSB,ion}}/\Delta x$) weighted by the corresponding $\mathrm{RBE}_{\mathrm{DSB}}$ value. $\mathrm{RBE}_{\mathrm{DSB}}$ data stem from PARTRAC monte carlo simulations (black) and experiments (red), respectively. Right column: numbers of DSB clusters per ion track length ($N_{\mathrm{DSB\ cluster}}/\Delta x$) as obtained from PARTRAC calculations. These values are reduced relative to the values of the middle column by the average number of DSBs found within one cluster. A simple geometric estimation concerning directly hit chromatin fibers (further explanation in the text) is also shown in the right column (blue).

numbers of DSBs per path length obtained from linear approximation (compare right and left column).

One can also estimate the minimum number of expected DSB clusters per track length considering the volume fraction of 5% occupied by chromatin fibers. For dense ion tracks, where each hit of a fiber by the track center should lead to the generation of a DSB site, counting simply the number of these hits leads to an average of about 1.4 predicted DSB sites per μm (see also right column in Figure 14).

To investigate the relationship between expected DSB sites and repair protein foci HeLa cells were irradiated by 29 MeV ^{7}Li and by 24 MeV ^{12}C ions at an angle of about 10° to the image plane of the epifluorescence microscope. Using an interpolation between the PARTRAC data the number of DSB clusters is predicted as 1 to 1.5 clusters per μm for 29 MeV ^{7}Li and as 3–4 clusters per μm for 24 MeV ^{12}C ions. Considering the optical resolution during fluorescence analysis and the extension of foci one would expect a more or less continuous line in the fluorescence micrograph along the tracks for the last-mentioned ion type. Our experiments show a much lower linear focus density than expected (Figure 15), namely on average about 0.8 foci per μm for both kinds of ions, albeit with a large statistical variation. Note that the counting of foci is difficult because of the presence of sub-structures visible at the larger foci where several small foci might be resolvable in higher resolution micrographs. These sub-structures might be due to clustering of foci by diffusion within the nucleus of the living cell to form larger foci several minutes after irradiation (Aten et al., 2004). Another reason for the larger than expected distance between the foci may lie in an additional higher order organisation of the chromatin. A recent model (Cremer et al., 2006) based on high resolution fluorescence images and electron microscopy proposes that the chromatin occupies small domains of high chromatin density while an interchromatin compartment consisting of channel- and lacuna-like structures separates the chromatin domains (for an illustration, see Figure 16). Such a gross structure would enhance the number of DSBs per cluster, resulting in larger clusters, but in a lower number of separated clusters.

4. Future Prospects

The most important advantage of Monte Carlo calculations over analytical models is the capability to include the microscopic dose fluctuations caused by secondary electron cascades and their end points where the electron energy loss is largest. In order to obtain reliable data for DSB induction and distribution, accurate differential cross sections for the electronic interaction of energetic ions in matter

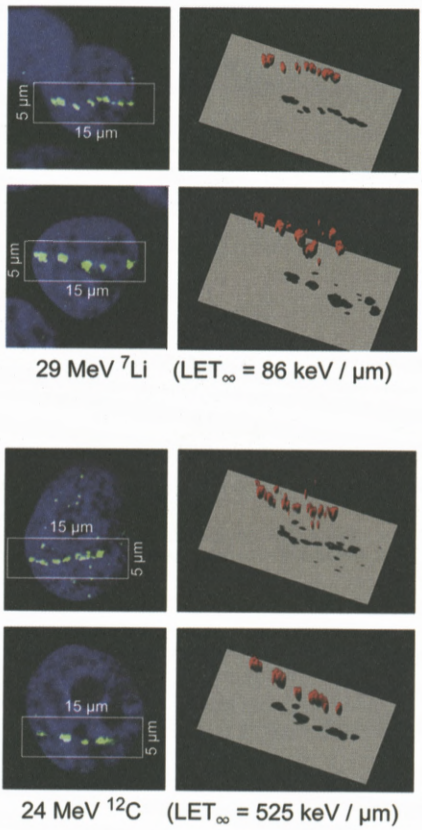

Figure 15. Left side: fluorescence micrographs (optical slices) of HeLa cell nuclei irradiated with single 29 MeV ^{7}Li or 24 MeV ^{12}C ions, respectively. The direction of the ion tracks encloses an angle of 10° with the image plane. 15 min after irradiation the cells were fixed and 53BP1 DNA repair factor accumulations were visualised by indirect immunofluorescence (green signal). Image stacks were taken using a motorized epifluorescence microscope and processed by deconvolution software. Right side: Corresponding three-dimensional reconstructions of image stacks were performed for the immunofluorescence signal using rendering software. The foci structures (red colour) of the DNA repair factor accumulations along the ion tracks reveal the distribution of DSB sites at the time of cell fixation.

and a realistic model for the DNA organisation within cell nuclei are needed. In particular, the present disagreement observed between calculations and observations of longitudinal DSB distributions along ion tracks may reflect a higher-order chromatin organisation that has not yet been adequately considered in the Monte Carlo approaches.

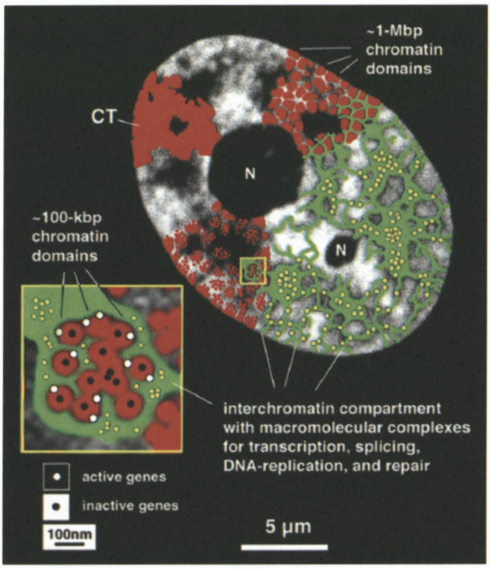

Figure 16. Chromosome territory-interchromatin compartment (CT-IC) model (Cremer et al., 2006). This model emphasizes that chromosomes occupy distinct territories in the cell nucleus. Chromosome territories (CTs) are built up from focal chromatin domains representing higher order chromatin structures with a DNA content in the range of about 10^6 base pairs. Each of these chromatin domains is thought to consist of a series of chromatin loop domains of about 10^5 base pairs. The model also emphasizes the presence of an interchromatin compartment (IC) with the most peripheral branches connected to the nuclear pores and protruding to the nuclear interior both between neighbouring CTs and into the interior of individual CTs. Actively transcribed genes locate at the chromatin surfaces exposed to the IC which contains nuclear bodies involved in various functions like transcription, splicing, replication and repair.

From the physical viewpoint, DSB induction is a certain endpoint resulting from interaction processes of ionising radiation with tissue. The energy transfers through ionisation, excitation and radical formation are the starting points which may end in the creation of DSBs. After completion of this physical and chemical stage within a timescale of nanoseconds biological processes occupied with the answer to the DNA damage take place in the living cell. Although a lot of DNA repair factors have been identified over the last decade, little is known on the spatiotemporal organisation of DSB repair, especially with respect to the structural organisation of DSBs within the cell nuclei. Even simple questions are not yet answered: Are there certain repair factories in the cell nucleus where damaged DNA is treated by the repair factors? Are the repair factories created at the damaged chromatin or has the damaged chromatin to move to the repair centers? What is the dynamical behaviour of the foci which are known to be formed by a number

of repair factors around DSBs? Do the foci move around and at what speed? What is the sequence of recruitment of repair factors, which one is earliest, which repair factors depend on each other?

These questions may be answered by radiation biology experiments preferentially performed at high energy ion microprobes. There the damaging action of ionising radiation can be induced by targeted irradiation which makes the cellular follow-up reactions accessible in space and time.

Acknowledgements

The experimental part of this work was supported by DFG grants Do438/9 and Cr59/23-1 as well as by the Maier Leibnitz Laboratorium of the TU-München and the Ludwig-Maximilians-Universität München.

References

Aten J.A., Stap J., Krawczyk P.M., Van Oven C.H., Hoebe R.A., Essers J. and Kanaar R. (2004): Dynamics of DNA double-strand breaks revealed by clustering of damaged chromosome domains. Science **303** (5654), 92–95

Berger M.J., Coursey J.S., Zucker M.A. and Chang J. (2005): Stopping-power and range tables for electrons (ESTAR) [online]. National Institute of Standards and Technology (NIST), Physics Laboratory, Gaithersburg, Maryland, USA. Available from: http://physics.nist.gov/PhysRefData/Star/Text/ESTAR.html (accessed 28 September 2006)

Bernhardt P. (2002): Strukturierte Targets in der Modellierung von strahlungsinduzierten DNS Schäden. Thesis (PhD), Technical University of Munich

Butz J.J. and Katz, R. (1967): Theory of RBE for heavy ion bombardment of dry enzymes and viruses. Rad Res **30**, 855–871

Chatterjee A. and Schaeffer H.J. (1976): Microdosimetric structure of heavy ion tracks in tissue. Rad Env Biophys **13**, 215–227

Chen J., Kellerer A.M. and Rossi H.H. (1994): Radially restricted linear energy transfer for high-energy protons: a new analytical approach. Rad Env Biophys **33**, 181–187

Cremer T., Cremer M., Dietzel S., Müller S., Solovei I. and Fakan S. (2006): Chromosome territories – A functional nuclear landscape. Curr Opin Cell Biol **18, no. 3**, 307–316

Datzmann G., Dollinger G., Goeden C., Hauptner A., Körner H.J., Reichart P. and Schmelmer O. (2001): The Munich microprobe SNAKE: First results using 20 MeV protons and 90 MeV sulfur ions. Nucl Instr Meth Phys Res B **181, nos 1–4**, 20–26

Dingfelder M. (2002): Cross section calculations in condensed media: Charged particles in liquid water. Radiation Protection Dosimetry **99, no. 1**, 23–27

Dingfelder M., Hantke D., Inokuti M. and Paretzke H.G. (1998): Electron inelastic-scattering cross sections in liquid water. Rad Phys Chem **53, no. 1**, 1–18

Fischer B.E. (1985): The scanning heavy ion microprobe at GSI. Nucl Instr Meth Phys Res B **10/11, no. 2**, 693–696

Fischer B.E., Heiss M. and Cholewa M. (2003): About the art to shoot with single ions. Nucl Instr Meth Phys Res B **210**, 285–291

Folkard M., Vojnovic B., Prise K.M., Bowey A.G., Locke R.J., Schettino G. and Michael B.D. (1997): A charged-particle microbeam: I. Development of an experimental system for targeting cells individually with counted particles. Int J Rad Biol **72, no. 4**, 375–385

Folkard M., Vojnovic B., Hollis K.J., Bowey A.G., Watts S.J., Schettino G., Prise K.M. and Michael B.D. (1997): A charged-particle microbeam: II. A single-particle micro-collimation and detection system. Int J Rad Biol **72, no. 4**, 387–395

Friedl A.A., Quicken P. and Kellerer A.M. (2003): Analyse räumlich korrelierter DNA-Schäden zur Bestimmung der relativen biologischen Wirksamkeit dicht-ionisierender Strahlung (BMU – 2003-616) [online]. Bundesministerium für Umwelt, Naturschutz und Reaktorsicherheit, Germany. Available from: http://www.bmu.de/strahlenschutz/doc/text/2476.php (accessed 28 September 2006)

Friedland W., Jacob P., Paretzke H.G. and Stork T. (1998): Monte Carlo simulation of the production of short DNA fragments by low-linear energy transfer radiation using higher-order DNA models. Rad Res **150**, 170–182

Friedland W., Jacob P., Paretzke H.G., Merzagora, M. and Ottolenghi, A. (1999): Simulation of DNA fragment distributions after irradiation with photons. Rad Env Biophys **38, no. 1**, 39–47

Friedland W., Jacob P., Bernhardt P., Paretzke H.G. and Dingfelder M. (2003): Simulation of DNA damage after proton irradiation. Rad Res **159, no. 3**, 401–410

Friedland W., Dingfelder M., Jacob P. and Paretzke H.G. (2005): Calculated DNA double-strand break and fragmentation yields after irradiation with He ions. Rad Phys Chem **72, nos 2–3**, 279–286

Greif K.D., Brede H.J., Frankenberg D. and Giesen U. (2004): The PTB single ion microbeam for irradiation of living cells. Nucl Instr Meth Phys Res B **217, no. 3**, 505–512

Hall E.J. (2000): Radiobiology for the Radiologist, 5th edn. Philadelphia: Lippincourt Williams & Wilkins.

Hauptner A., Dietzel S., Drexler G.A., Reichart P., Krücken R., Cremer T., Friedl A.A. and Dollinger G. (2004): Microirradiation of cells with energetic heavy ions. Rad Env Biophys **42, no. 4**, 237–245

IAEA (1995): Atomic and molecular data for radiotherapy and radiation research (IAEA-TECDOC-799), page 440 [online]. IAEA (International Atomic Energy Agency), Vienna, Austria. Available from: http://www-pub.iaea.org/MTCD/publications/PDF/te_799_prn.pdf (accessed 28 September 2006)

Jakob B., Scholz M. and Taucher-Scholz G. (2003): Biological imaging of heavy charged-particle tracks. Rad Res **159, no. 5**, 676–684

Krämer M. and Kraft G. (1994): Calculations of heavy-ion track structure. Rad Env Biophys **33, no. 2**, 91–109

Michael B.D. and O'Neill P. (2000): A sting in the tail of electron tracks. Science **287** (5458), 1603–1604

Nikjoo H., O'Neill P., Terrissol M. and Goodhead D.T. (1999): Quantitative modelling of DNA damage using Monte Carlo track structure method. Rad Env Biophys **38, no. 1**, 31–38

Randers-Pehrson G., Geard C.R., Johnson G., Elliston C.D. and Brenner D.J. (2001): The Columbia University single-ion microbeam. Rad Res **156, no. 2**, 210–214

Xapsos M.A. (1992): A spatially restricted linear energy transfer equation. Rad Res **132**, 282–287

Ziegler J.F. and Biersack J.P. (2003): The stopping and range of ions in matter (SRIM2003) [online]. Available from: http://www.srim.org (accsessed 28 September 2006)